ILASS – Europe 2016, 27th Annual Conference on Liquid Atomization and Spray Systems, 4-7 September 2016, Brighton, UK

Modelling of the Evolution of a Droplet Cloud in a Turbulent Flow

Andreas Papoutsakis [*1], Oyuna Rybdylova [1], Timur Zaripov [1], Luminita Danaila [2], Sergei S. Sazhin [1]

[1] Sir Harry Ricardo Laboratories, School of Computing, Engineering and Mathematics, University of Brighton, Brighton BN2 4GJ, UK

[2] CORIA, UMR 6614, Université de Rouen, Avenue de l'Université, BP 12, 76801 Saint Etienne du Rouvray, France

*Corresponding author: a.papoutsakis@brighton.ac.uk

Abstract

In this work we examine the effect of turbulent mixing on the droplet number density for a cloud of droplets dispersing in a turbulent flow field. The Lagrangian droplets are assumed to be transported and dispersed by the large scale structures of a resolved field. However, turbulent fluctuations not visible to the filtered solution induce unresolved dispersion of droplets within a droplet cloud. The Fully Lagrangian Approach (FLA) is used to model resolved droplet dispersion. A model is presented for the prediction of the unresolved turbulent mixing of the droplet number density for a droplet cloud. This model takes into account the turbulent flux for the droplets permeating the surface of the cloud via turbulent diffusion. Turbulent diffusion is assumed to be driven by the kinetic energy of the droplet fluctuations induced by the turbulent kinetic energy of the carrier phase. This assumption is supported by Direct Numerical Simulations (DNS) of homogeneous and isotropic turbulence. Additionally, DNS of transition of a planar jet to turbulence is used for the assessment of the mixing model which we use. The calculation of the spatial derivatives for the droplet number densities is performed by projecting the FLA solution on the Eulerian mesh, resulting in a hybrid Lagrangian-Eulerian approach to the problem.

Introduction

Particle (droplet) laden flows are encountered in a wide variety of applications, ranging from droplet dispersion in internal combustion engines during fuel injection to the prediction of droplet dispersion transport in environmental flows. The most widely used method in two-phase flow modelling is a combination of the Eulerian approach for the carrier-phase flow and the Lagrangian approach for the dispersed phase (Lagrangian-Eulerian approach) [1]. In [2], a Fully Lagrangian Approach (FLA) for finding the dispersed phase parameters, including the concentration, along droplet pathlines was proposed. Direct modelling of individual droplets in the carrier phase produces adequate results for droplet velocities [3]. However, it has been shown that accurate calculation of droplet concentrations requires an excessive number of individual droplets in order to predict statistically meaningful values of particle concentrations [4]. In [4] it was shown that the most efficient way to calculate this concentration (amongst those suggested so far) is based on the above-mentioned FLA in the form developed by Osiptsov (Osiptsov method) [2]. The original Osiptsov method was developed and tested for laminar flows of the carrier phase. Recently, it was used for the investigation of particle agglomeration properties in a homogeneous and isotropic turbulent flow [5] using Direct Numerical Simulation (DNS). In the present work, we intend to generalise the Osiptsov method to the analysis of particles in filtered turbulent flows. In real life applications it becomes computationally impossible to achieve the resolution required to fully acount for all the scales in a turbulent flow. Hence, filtering or averaging operators are imposed on the governing equations. This aims to reduce the complexity of the problem by avoiding the full resolution of the whole range of turbulent scales. Although turbulent diffusion in dispersed phase flows can be predicted in the Eulerian context, compressibility effects for high inertia particles introduce modelling challenges for the Eulerian approaches [6].

We focus on the mechanism of how the individual droplets are exchanged across the spatially averaged stream lines of droplet clouds. This mechanism is based upon turbulent fluctuations of droplets induced by turbulent fluctuations of the carrier phase. As a result, this induced unresolved motion of the dispersed phase is expected to lead to diffusion flux of droplets. This flux is driven by turbulent diffusion which is proportional to the spatial variation of the droplet number density.

Very accurate, simultaneous measurements of the carrier phase velocity field and the droplet distribution are needed in order to assess the validity of closures and modelling assumptions. Numerical experiments are best suited to retrieving the spatial structure of the turbulent flow field. Hence, DNS is better suited than experimental measurement to the evaluation of modelling methodologies. The simplest approach to assesssing the assumptions and the performance of the suggested model, is to apply it to the filtered flow fields. The latter are extracted from fundamental turbulent flow fields inferred from Direct Numerical Simulations. Additionally, we focus on the relation between the levels of turbulence in the dispersed and continuum phases.

Material and methods

The Fully Lagrangian Approach (FLA), used in our analysis, aims to model the dispersed phase in a point particle manner [2, 5]. We assume that the discrete phase is conveyed by the flow field of the carrier phase, described by velocity $\mathbf{U}$. The trajectory of the Lagrangian element is described by the following equations:

$$\frac{\partial x_i^d}{\partial t} = V_i \ , \tag{1}$$

$$m_i \frac{\partial V_i}{\partial t} = f_i \ . \tag{2}$$

Eqs. (1) and (2) describe the position $\mathbf{x}^d = \left(x_1^d, x_2^d, x_3^d\right)$ of a droplet, and its velocity $\mathbf{V} = (V_1, V_2, V_3)$ respectively. We assume that the only force acting on the droplet with mass m_i, is the drag force f_i induced by the velocity of the carrier phase U_i relative to the velocity of the droplet V_i. We restrict our analysis to the Stokesian limit $(Re_d < 1)$. In this case, Eq. (2) can be written as:

$$\frac{\partial V_i}{\partial t} = \frac{1}{\tau_d}(U_i - V_i) \ , \tag{3}$$

where, τ_d is the relaxation time of the droplet d, related to the droplet Stokes number $St = \tau_d / t_0$. The droplet relaxation time is defined as:

$$\tau_d = \frac{\rho_d d_d^2}{18 \mu_c} \ , \tag{4}$$

ρ_d is the droplet material density, d_d is the diameter of the droplet and μ_c is the dynamic viscosity of the carrier phase.

FLA, introduced by Osiptsov [2], considers the dispersed phase as a continuum. Following Osiptsov [2] the mass conservation in Lagrangian coordinates is presented as follows:

$$n_d(\mathbf{x}_0, t)|det(J(\mathbf{x}_0, t)| = n_d(\mathbf{x}_0, 0) \ , \tag{5}$$

where $n_d(\mathbf{x}_0, t)$ is the local droplet number density, $|det(J(\mathbf{x}_0, t)|$ is the absolute value of the determinant of the Jacobian of the transformation from the Eulerian to Lagrangian coordinates. This is defined as:

$$J_{ij} = \frac{\partial x_i^d}{\partial x_{0,j}^d} \ , \tag{6}$$

where, x_i^d is the ith component of the current position vector of the droplet cloud at time instant t, $x_{0,j}^d$ is the jth coordinate of the position of the droplet at the initial time instant $t = 0$. The initial position vector $\mathbf{x}_0^d$ and time t are the Lagrangian coordinates of the droplet d. The determinant of the Jacobian matrix $|det(J_{ij})|$ in Eq. (5) describes the distortion of the dispersed phase volume. Following FLA, the entries of the Jacobian matrix J_{ij} are calculated by solving the initial value problem:

$$\frac{\partial J_{ij}}{\partial t} = \omega_{ij} \ , \tag{7}$$

$$\frac{\partial \omega_{ij}}{\partial t} = \frac{1}{\tau_d}\left(J_{kj}\frac{\partial U_i}{\partial x_k} - \omega_{ij}\right) \ , \tag{8}$$

where ω_{ij} is the auxiliary variable.

As follows from Eq. (5), the Osiptsov method provides an explicit expression for the number density (concentration) of droplets using the Jacobian of the Lagrangian transformation acting as a measure of the droplet cloud deformation. For a turbulent flow field, modelled under the Large Eddy Simulation (LES) context, the carrier phase velocity field is decomposed to the spatially filtered value $\boldsymbol{U}$ and the sub-grid contribution $\boldsymbol{u}'$:

$$\boldsymbol{U} = \overline{\boldsymbol{U}} + \boldsymbol{u}' \ , \tag{9}$$

where the operator $\bar{\cdot}$ stands for the spatially filtered value. In the analysis presented here the simple box filter is assumed:

$$\overline{f}(\boldsymbol{x}_0, t) = \frac{1}{\Delta^3} \int_{V_e} f(\boldsymbol{x}, t) d\boldsymbol{x} \ . \tag{10}$$

The above operation results in a spatially averaged value over the computational element volume V_e characterised by the filter width $\Delta = V_e^{1/3}$. In a spatially filtered flow field, dispersed droplets are expected to deviate from the trajectory inferred from the averaged solution, due to turbulent fluctuations, leading to turbulent mixing of droplets as shown in Figure 1. For a droplet cloud within a Lagrangian volume V, the mass conservation can be written in the following integral form:

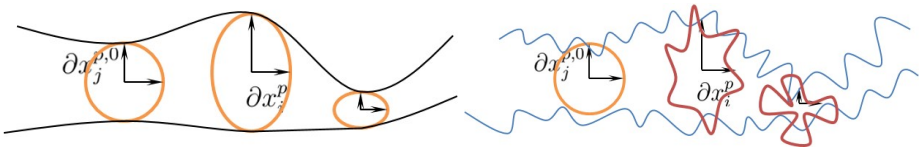

Figure 1. Left: Schematic of the evolution of a droplet cloud element within a filtered flow field. **Right:** Schematic of the evolution of a droplet cloud element within a turbulent flow field.

.

$$\frac{d}{dt} \int_V n_d(\mathbf{x}, t) d\boldsymbol{x} = 0 \ . \tag{11}$$

This equation shows that the integral of the number density $n_d(\mathbf{x}, t)$ in a cloud of droplets remains constant. The same is valid for droplets transporting in the averaged flow field. However, if we take into account unresolved turbulent fluctuations of the carrier phase we can expect that due to the induced turbulent droplet motions droplets can permeate the surface S_L enclosing volume V_L of the droplet cloud. Thus, Eq. (11) can be generalised to:

$$\frac{d}{dt} \int_{V_L} n_d(\mathbf{x}, t) d\boldsymbol{x} = - \int_{S_L} \mathbf{F}^{turb} \mathbf{n} dS_L = - \int_{V_L} \nabla \cdot \mathbf{F}^{turb} d\boldsymbol{x} \ . \tag{12}$$

where the RHS takes into account turbulent diffusion of droplets due to the unresolved turbulent fluctuations. $\mathbf{F}^{turb}$ is the turbulent flux of droplets migrating through the cloud surface per unit of time. Introducing the Lagrangian coordinates $\mathbf{x_0}, t$, Eq. (12) is expressed in the following Lagrangian form:

$$\frac{d}{dt} \int_{V_0} n_d(\mathbf{x_0}, t) \left| det\left(\overline{J_{ij}}(\mathbf{x}_0, t)\right)\right| d\boldsymbol{x}_0 = - \int_{V_0} \nabla \cdot \mathbf{F}^{turb} \left| det\left(\overline{J_{ij}}(\mathbf{x}_0, t)\right)\right| d\boldsymbol{x}_0 \ , \tag{13}$$

integrated over an initial elementary unit volume $V_0 = V(t = 0)$. Since, Eq. (13) is valid for any arbitrary volume, we obtain the following generalised form of the equation for the droplet number density:

$$\frac{d}{dt} \left[n_d(\mathbf{x}_0, t) \left| det\left(\overline{J_{ij}}\right)\right| \right] = - \left| det\left(\overline{J_{ij}}\right)\right| \nabla \cdot \mathbf{F}^{turb} \ , \tag{14}$$

where $\left| det\left(\overline{J_{ij}}\right)\right|$ is the Jacobian of the transformation from the Eulerian $\mathbf{x}$ to the Lagrangian $\mathbf{x}_0$ coordinates inferred from the filtered flow field $\overline{\boldsymbol{U}}$. The individual droplets in the cloud are characterised by a mean droplet velocity $\overline{\boldsymbol{V}}$ which governs the filtered trajectory of the cloud as predicted by Eqs. (1) and (2). Using the averaged droplet velocity the velocities of the individual droplets can be decomposed to the averaged value $< \boldsymbol{V} >$ and their individual contribution $\boldsymbol{v}'$ as:

$$\boldsymbol{V} = < \boldsymbol{V} > + \boldsymbol{v}' \ , \tag{15}$$

The energy of the individual droplet velocity fluctuations $k_v = 0.5 < \boldsymbol{v}' \cdot \boldsymbol{v}' >$ can be used to define a characteristic velocity of the droplet fluctuations $\mathcal{V} = \sqrt{2/3 k_v}$. The turbulent flux $\mathbf{F}^{turb}$ is assumed to be driven by the Fickian diffusion induced from the individual droplet fluctuations. Assuming a turbulent mixing model, turbulent viscosity can be considered proportional to the characteristic velocity of the turbulent fluctuations $\mathcal{V}$, the characteristic length $\mathcal{L}$, and finally the gradient of the slowly varying component $\nabla \overline{n}_d$ of the droplet number density distribution:

$$\mathbf{F}^{turb} = -\mathcal{V}\mathcal{L}\nabla n_d = -\lambda\mathcal{U}\mathcal{L}\nabla\overline{n}_d \ , \tag{16}$$

where λ is the ratio of the characteristic droplet velocity $\mathcal{V}$ and the characteristic velocity of the carrier phase $\mathcal{U}$: $\lambda = \mathcal{V}/\mathcal{U}$. The carrier phase characteristic velocity stems from the subgrid turbulent kinetic energy $k_{sgs} = 0.5\overline{\boldsymbol{u}' \cdot \boldsymbol{u}'}$ of the carrier phase fluctuations as $\mathcal{U} = \sqrt{2/3k_{sgs}}$. Introducing the concept of turbulent viscosity, the product $\mathcal{U}\mathcal{L}$ is replaced by ν_t. Integrating Equation (14) over time and taking into account Equation (16) we obtain the following expression for the droplet number density:

$$n_d(\mathbf{x}_0, t) = \frac{n_d(\mathbf{x}_0; 0)}{\left|det\left(\overline{J_{ij}}(\mathbf{x}_0, t)\right)\right|} + \frac{1}{\left|det\left(\overline{J_{ij}}(\mathbf{x}_0, t)\right)\right|} \int_{\tau=0}^{\tau=t} \left|det\left(\overline{J_{ij}}(\mathbf{x}_0; \tau)\right)\right| \nabla \cdot \left(\lambda\nu_t \nabla\overline{n}_d\left(\mathbf{x}_0; \tau\right)\right) d\tau \ , \tag{17}$$

λ can be estimated using the intensity of droplet fluctuations as a function of the turbulent intensity of the carrier phase $\mathcal{U}$. A closure for $\mathcal{V}$ can be achieved by introducing the Stokes law in the expression for the characteristic velocity $\mathcal{V}$ of droplet fluctuations:

$$\frac{d\mathcal{V}^2}{dt} = \frac{1}{3}\frac{d}{dt}\overline{v_i' v_i'} = \frac{1}{3}\overline{2v_i' \frac{dv_i'}{dt}} = \frac{2}{\tau_d}\left(\frac{1}{3}\overline{v_i' u_i'} - \frac{1}{3}\overline{v_i' v_i'}\right). \tag{18}$$

The modulation term $\frac{1}{3}\overline{v_i' u_i'}$ is bounded in $[0, \mathcal{U}^2]$ [7] and is modelled as:

$$\frac{1}{3}\overline{v_i' u_i'} = \mathcal{U}^2 e^{-B\tau_d/\tau_t}. \tag{19}$$

Hence,

$$\frac{d\mathcal{V}^2}{dt} = \frac{2}{\tau_d}\mathcal{U}^2\left(e^{-B\frac{\tau_d}{\tau_t}} - \lambda^2\right) \ , \tag{20}$$

where τ_t is the turbulent characteristic time. B is an empirical constant set equal to $B = 0.5$ [8, 9]. Eq. (20) provides the rate of change of the droplet fluctuation intensity accounting for the dynamic response of droplets to the carrier phase turbulent fluctuations. In the LES approach the expression for ν_t is inferred from the Smagorinsky model:

$$\nu_t = (c_S\Delta)^2|\overline{S}| \ , \tag{21}$$

where c_S is the Smagorinsky constant and $|\overline{S}| = \sqrt{2S_{ij}S_{ij}}$ is the magnitude of the resolved rate of strain tensor. Δ is a length scale inferred from the size of the filtering volume V: $\Delta = V^{1/3}$. A typical value of the Smagorinsky constant, $C_S = 0.2$ (see [10, 11, 12]), is used in our analysis. Note that some authors, including Deardoff [13] and Schumann [14], argued that a value of 0.2 for the Smagorinsky constant is too dissipative (see [15]) for channel flows and suggested $C_S = 0.1$.

Results and discussion

In this section we present the results of testing the model using the flow field produced by our DNS code, which was spatially filtered using the box filter. The assumptions and functionality of the diffusion mechanism will be assessed. The driving force behind turbulent diffusion is the unresolved fluctuations of individual droplets. The starting point for our analysis will be investigation of the relation between the droplet and carrier phase fluctuations: $\mathcal{V}$ and $\mathcal{U}$.

The droplet dispersion simulations in the turbulent flow fields are characterised by two distinct types of initialisations for the velocity flow field representing two typical families of these fields. The first one refers to a homogeneous and isotropic turbulence flow field. The aim of this simulation is to investigate the closure of the droplet characteristic velocity as described by Eq. (18). The input parameters for this first family of simulations are presented in Table 1. The second initialisation refers to a planar jet. The corresponding family of simulations is focused on DNS cases describing the transition of a laminar planar jet to a fully turbulent flow. The results of the calculations, spatially filtered, are used as a carrier phase flow field in our model. The input parameters and characteristics for the planar jet simulations are presented in Table 2.

The most straightforward approach to predicting the evolution of a turbulent flow field is DNS, where a direct numerical solution of the governing equations is carried out. This approach is common in the analysis of laminar stationary flow fields. However, turbulent flow fields present great variety of scales which extend to much smaller length scales than the scales of the boundary conditions and the macroscopic characteristics of the flow. Simulations of turbulent flow fields must account for all the scales of turbulent fluctuations. Thus, the numerical discretisation in this case must be smaller than the smallest turbulent length scale.

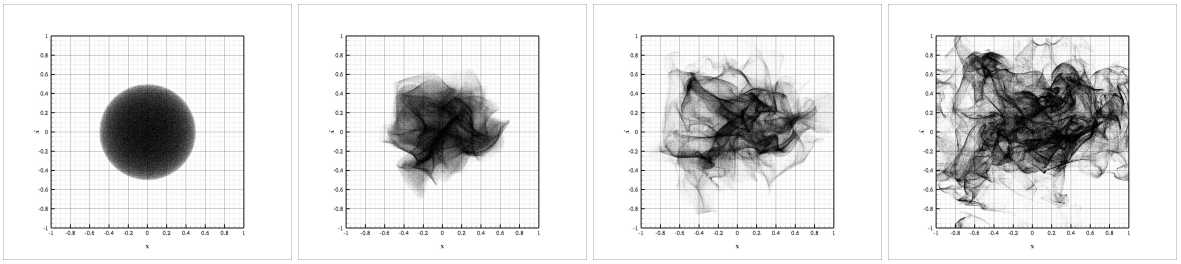

Figure 2. An evolution of a subset of individual droplets initially located within a spherical volume. The results of calculation were extracted from the simulation of droplet dispersion in homogeneous and isotropic turbulence for dimensionless times $t^* = 0$, 1, 1.5 and 2. $St = 0.1$.

Table 1. Homogeneous turbulence cases consisting of two sets of decaying and forced simulations for three Stokes numbers. All cases were run for the same initial turbulent flow field characterised by the Taylor microscale Reynolds number $Re_T = 54$. The carrier phase was discretised with 256^3 nodes and $8 \cdot 10^5$ individual droplets were used for the simulation of the dispersed phase.

Case	St	Forcing
HF01	0.1	Yes
HF02	0.2	Yes
HF05	0.5	Yes
HD01	0.1	No
HD02	0.2	No
HD05	0.5	No

The momentum transport is solved, using the pseudospectral code described in [16], for a cubic domain of size 2π and periodic boundary conditions in all three directions. The solver is based on the integration of the incompressible Navier-Stokes equations in the spectral space. The nonlinear terms of the Fourier basis functions arising from the evaluation of the convection terms of the momentum transport are evaluated in the physical space. To achieve this, a Real Fast Fourier Transform (RFFT) and two Complex FFT's (CFFT) are applied to retrieve the flow field in the spectral space. The transformation to the physical space is achieved using the same series of inverse transformations. The alias errors occurring during the Fourier transformations are removed using the $2/3$ rule, where the high wavenumber part of the spectrum is ignored [17].

Table 2. Planar jet simulation cases. All simulations were performed for $8 \cdot 10^5$ individual droplets with $St = 0.1$.

Case	discretisation	Re_D	No. of averaging volumes	No. of droplet clouds
J1D4S01	256^3	3142	4	4
J1D8S01	256^3	3142	8	8
J1D16S01	256^3	3142	16	16
J3D8S01	512^3	6283	8^3	8^3
J3D16S01	512^3	6283	16^3	16^3

In the pseudospectral code, periodicity is strongly imposed by the selection of the Fourier basis functions. Although periodicity restricts the variety of problems that can be solved using the pseudospectral code, periodic boundary conditions do not prevent us from carrying out realistic simulations of turbulent flows. Indeed, for non-periodic simulations of turbulence, producing artificial turbulence to simulate non-periodic inflow conditions is a complicated task [18] which may introduce inaccuracies, interfering with the turbulent statistics, especially close to the inflow and outflow boundaries.
On the other hand, the initial conditions for homogeneous isotropic turbulence calculations are defined from artificially composed synthetic turbulence using the spectral reconstruction method [17]. According to this method, the initial flow field is considered as a result of superposition of Fourier modes. The intensity of the modes for each wavenumber vector $\boldsymbol{k}$ is a function of the energy spectrum [19]:

$$E(|\mathbf{k}|) = c|\mathbf{k}|^4 e^{-|\mathbf{k}|^2/a^2} \ , \tag{22}$$

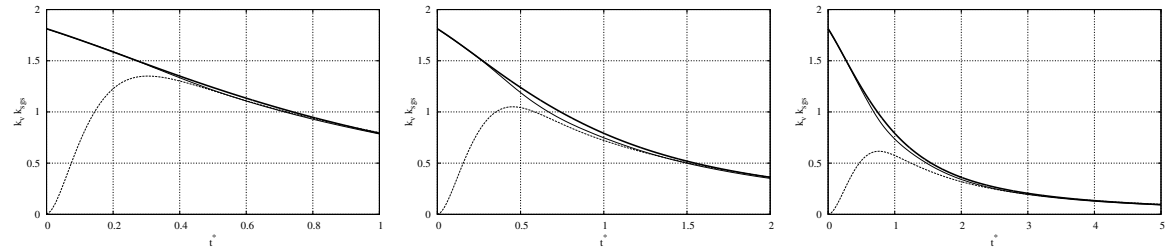

Figure 3. Time evolution of the kinetic energy of fluctuations of the droplet velocity (dashed lines), the intensity of carrier flow velocity fluctuations (solid lines) and the intensity of carrier flow fluctuations encountered by the droplets (thin solid line) for the simulations of decaying homogeneous and isotropic turbulence. Three Stokes numbers, St=0.1 (far left), 0.2 (middle) and 0.5 (far right) were used.

where constants c and a are chosen in such a way that all scales of the resulting turbulent flow field are well resolved [20]. An indication of the adequate resolution of the flow field is monotonic decay of the turbulent spectrum and the fact that the energy of the smallest scales is minimal. The phase for each of these modes is then chosen randomly, subject to consistency with the mass conservation equation [21]. A synthetic turbulent flow field is constructed using Eq. (22). Thus, it is not characterised by an organised inertial range and does not respect high order velocity correlations [17]. In order to derive a homogeneous isotropic turbulent flow field, the synthetic flow field is integrated, while the large eddies are maintained by forcing. The forcing procedure mimics the energy cascade from larger to smaller scales. This results to the maintenance of a fully turbulent flow field, avoiding its decay due to viscosity. In the cases which we simulated, the forcing is implemented by artificially increasing the energy of the fluctuations for the two lowest wavenumbers $|\boldsymbol{k}| = 1$ and $|\boldsymbol{k}| = 2$ when the total turbulent kinetic energy becomes smaller than its initial value. This lasts for seven eddy turnover times. The resulting initial condition for the homogeneous simulations is characterised by a Reynolds number (based on the Taylor microscale λ_T and the characteristic velocity $\mathcal{U}$) $Re_T = 54$. The definition of the Taylor microscale is based on the two point velocity correlation coefficient and provides the lower limit of the integral length scale. Here it is calculated from the turbulent kinetic energy $3/2\mathcal{U}^2$ and the dissipation rate ϵ as:

$$\lambda_T = \sqrt{15\nu\frac{\mathcal{U}^2}{\epsilon}}\,. \tag{23}$$

where ν is the molecular viscosity of the fluid.

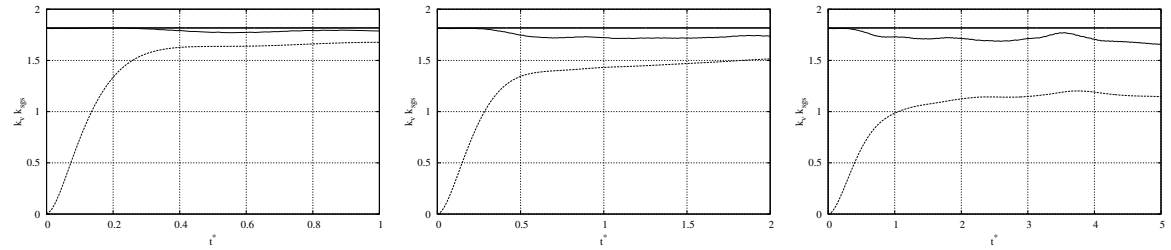

Figure 4. Time evolution of the kinetic energy of fluctuations of the droplet velocity (dashed lines), the mean flow velocity fluctuations (solid lines) and the intensity of carrier flow fluctuations encountered by the droplets (thin solid line) for the simulations of forced homogeneous and isotropic turbulence. Three sets of Stokes numbers, St=0.1 (left), 0.2 (middle) and 0.5 (right) were used.

The dispersed phase is modelled using a statistically significant number of individual droplets. In the homogeneous turbulence simulations presented in this paper the droplets are initially quiescent and randomly scattered throughout the cubic domain. Starting from their initial positions, droplets begin to move due to fluctuations in the carrier phase as shown in Figure 2 for four different dimensionless times $t^* = t/t_0$. The initial value problem described by Eqs. (1) and (2) is integrated over time using the same minimal storage time-advancement third order Runge-Kutta scheme as in [22]. The latter is also used for the integration of the flow field. In this algorithm, three realisations of flow field at equal intermediate time steps are used to provide the final prediction. Drag induced by the turbulent flow is calculated following Eq. (3). The interactions between the droplets and the effect of droplets on the carrier phase are ignored assuming low mass load of the dispersed phase.

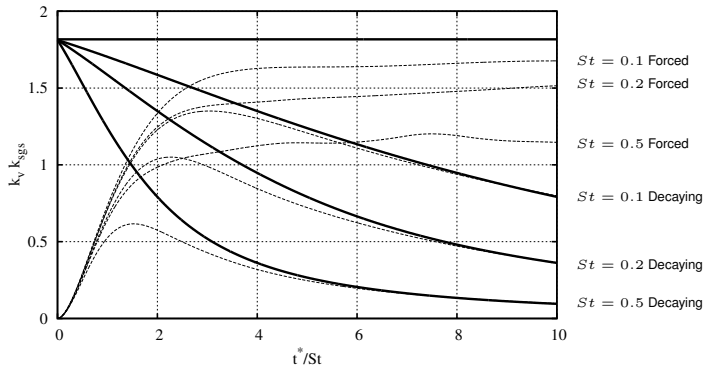

Figure 5. Kinetic energies of fluctuations of dispersed (dashed) and carrier phase (solid) versus nomalised (by St) time. Forced (horizontal solid line) and unforced cases are shown. Three sets of Stokes numbers, St=0.1 (upper curves), 0.2 (middle curves) and 0.5 (lower curves) were used. In unforced cases the kinetic energies of the carrier and dispersed phases converge at long times as shown earlier. At the initial stage the kinetic energies of the dispersed phase are the same for all Stokes numbers.

For individual droplet simulations, the main computational effort is required when tracking the positions of droplets and the values of the components of the carrier phase velocities at the location of the droplets. In the spectral algorithm used in our analysis, the carrier phase flow field in the physical space is accessed in two dimensional slices during calculations of nonlinear convection terms. Thus, the tracking algorithm is restricted to iso-z slices of the computational domain. Droplets are sorted according to their positions along the curve filling the whole physical space. This curve covers the computational domain. The sequence in which the droplets are sorted is the same as the sequence of the retrieval of real space variables from the spectral space representation. Furthermore, the droplets are redistributed across the domain decomposition of the carrier phase resulting in a balanced distribution of droplets across the computational partitions. Finally, field variables at the exact droplet locations are extrapolated using a second order Taylor expansion of the spectral flow field solution.

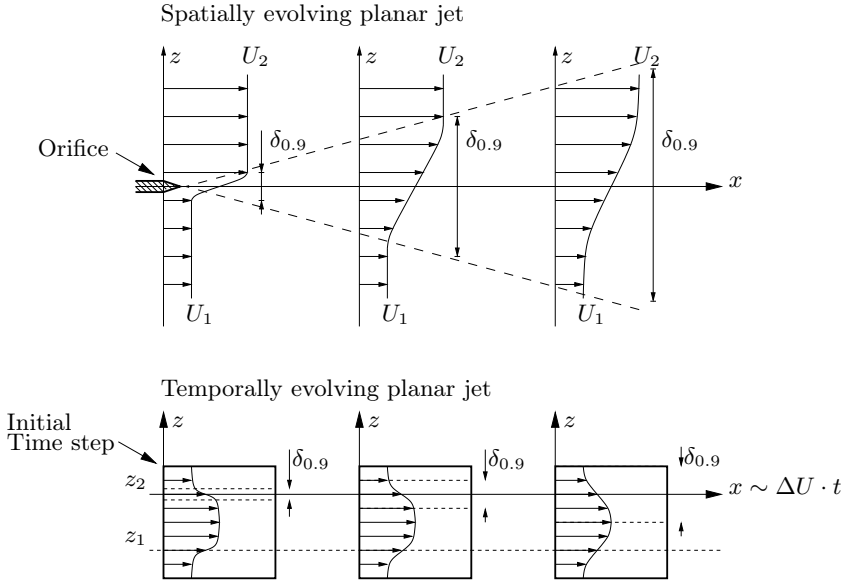

Figure 6. Schematics of the velocity profiles of a spatially evolving planar jet at three distances from the nozzle (top) and the schematics of the velocity profiles of a temporally evolving planar jet at three time instances (bottom).

For the three sets of decaying turbulence simulations `HD01` to `HD05`, shown in Table 1, the evolution of the turbulent kinetic energy for the carrier phase is shown in Figure 3. The turbulence intensity of the homogeneous and isotropic carrier phase flow field decays over time. This takes place due to the cascade of energy from the largest to the smallest scales where the energy dissipates due to viscosity. In the meantime, the initially quiescent droplets start to fluctuate under the effect of the turbulent carrier phase flow field. The turbulence intensity of the dispersed phase reaches the levels of the turbulent kinetic energy of the carrier phase before it starts decaying together with the

carrier phase.
The forced turbulence simulations `HF01` to `HF05` aim to recreate the conditions within a computational cell of a filtered turbulent simulation where energy cascades from the larger scales to the smaller ones. This sustains sub-grid turbulence fluctuations. As shown in Figure 4, the droplet turbulence fluctuations asymptotically reach a plateau where the intensity of droplet fluctuations is below that of the carrier phase turbulent fluctuations. The dotted curves in Figure 4 show the fluctuations of the carrier phase encountered by the droplets. At the initial stage of the turbulent mixing of the droplets, the carrier phase turbulent kinetic energy, encountered by the droplets, is equal to the carrier phase turbulent kinetic energy. This happens since the droplets are randomly distributed within the flow field. As soon as the droplets have adapted to the carrier phase flow field fluctuations, their positions no longer represent the carrier phase flow field. This can be attributed to the fact that the droplets tend to avoid positions with higher fluctuation intensities. This behaviour becomes more visible for higher Stokes numbers. Due to the unsteady nature of the decaying turbulence simulations, this behaviour is not so evident for these cases. The initial adaptation stage of the droplets to the carrier phase turbulent flow field can be observed for all six simulations of decaying and forced turbulence, shown in Table 1, when the time scale is normalised by the stokes nunber St, as shown in Figure 5.

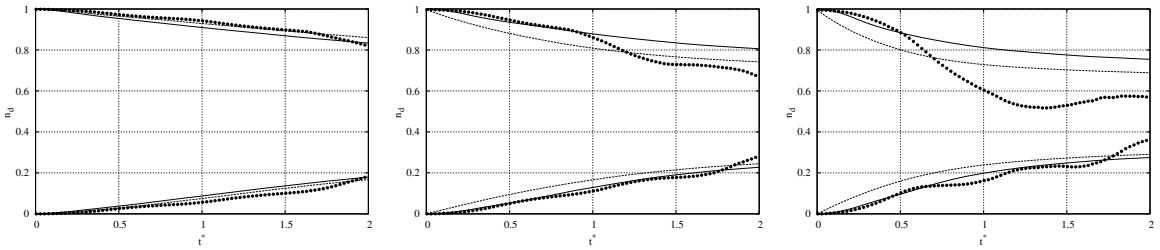

Figure 7. Droplet number density for cases `J1D4S01` to `J1D16S01` at two bilateral positions of the planar jet shear layer. Dotted curves: DNS averaged data, Dashed curves: droplet number density predicted by the model with $\lambda = 1$. Solid curves: droplet number density for $\lambda = \mathcal{V}/\mathcal{U}$ Left: 4 averaging volumes on the z-direction. Middle: 8 averaging volumes on the z-direction. Right: 16 averaging volumes on the z-direction.

In order to investigate the diffusion mechanism described by Eq. (17), DNS of planar jet configurations [23] have been carried out. The planar jet case is a simulation of a jet stream issuing into a quiescent fluid.
The initial conditions for the planar jet are illustrated in Figure 6. This figure shows a cross-section of the initial flow field on the iso-y plane. A hyperbolic tangent profile is used for the initialisation of the velocity. A similar setup was used by Stanley et al. [24], where a hyperbolic tangent profile was applied for the boundary conditions of the DNS for a spatially evolving planar jet. In the case presented in this study, the boundary conditions for all quantities are periodic in all directions as imposed by the spectral algorithm. In our simulations, a planar jet evolves over time rather than in space. The jet issues parallel to the x-axis, along the stream-wise direction. The velocity profile is specified along the z-axis defining the transverse direction. This configuration initially consists of two laminar shear layers. These layers are unstable and are expected to demonstrate a transitional stage from laminar to fully turbulent flow, when the two shear layers start merging. The initial parallel unidirectional profile is described by the following equation:

$$u(x,y,z;t=0) = \frac{\Delta U}{2}\left[\tanh\left(\frac{z-L/2}{2\delta_m}\right) - \tanh\left(\frac{z-3L/2}{2\delta_m}\right) - 1\right] , \tag{24}$$

where L is the width of the jet, δ_m is the initial momentum thickness of each mixing layer which controls the wavelength of the initial Kelvin Helholtz instability, and ΔU is the difference between the mean initial velocity of the two streams.
In order to trigger the instability of this shear flow, synthetic perturbations of 2% magnitude were superimposed on the velocity field. Similar perturbations were introduced as inflow boundary conditions for spatially evolving DNS of planar jets [24], or included in the initial conditions of the temporally evolving DNS of a mixing layer [25]. The macroscopic Reynolds number for the cases provided in Table 2 is defined as:

$$Re_D = \frac{\Delta U L}{\nu} . \tag{25}$$

The first three cases shown in Table 2 are characterised by the low Reynolds number $Re_D = 3141.5$ and are discretised using 256 physical nodes in each direction. The macroscopic Reynolds number for the last two cases is equal to $Re_D = 6283.0$ with computational mesh using 512 nodes in each direction. The two mixing layers lie in the vicinity of two iso-z planes, located at positions $z_1 = \pi/2$ and $z_2 = 3\pi/2$, respectively. The results of our DNS can be compared with experimental results referring to spatially evolving shear layers [26, 27].

In Figure 6 we show a comparison between the configuration of a spatially evolving planar jet and the configuration of a temporally evolving planar jet used for our DNS. Two streams issue from an orifice or splitter plate with almost uniform velocity profiles U_1 and U_2. The mean convection velocity of the mixing layer U_m is defined as $U_m = (U_1 + U_2)/2$, where U_1 and U_2 are the velocities of each stream. In contrast to the DNS of spatially evolving planar jets [28, 24], the simulation presented in this study evolves over time rather than in space.
The mixing layer is well known for its coherent structures [29]. During the first stage of transition, vorticity tubes, also known as rollers, appear [30]. These cylindrical regions are characterised by large vorticity magnitudes, show two dimensional structures and extend along the span-wise direction as predicted by the linear stability analysis for the Kelvin-Helmholtz instability [31]. During the later transitional stage, the vorticity tubes become interconnected with three dimensional structures, the so-called rib vortices.

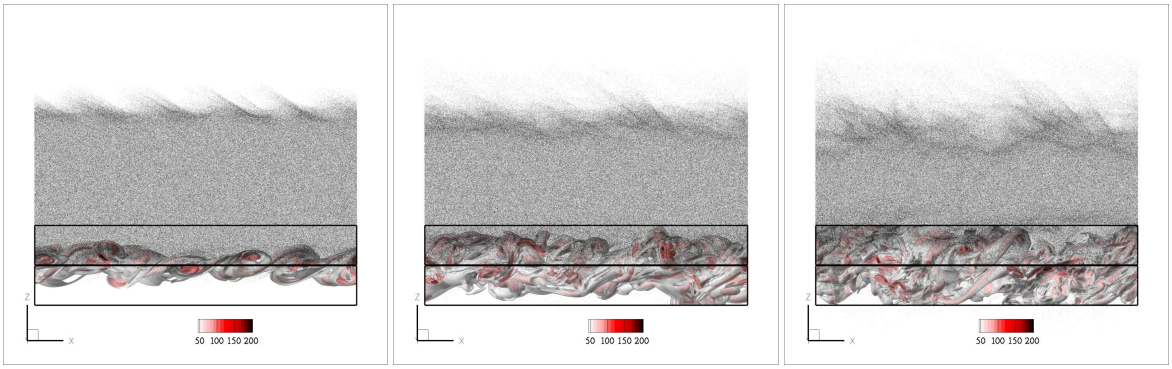

Figure 8. The evolution of the individual droplets dispersing in the planar jet configuration for three different realisations of the flow at dimensionless times $t^* = 0.270$, $t^* = 0.423$ and $t^* = 0.575$. The iso-surfaces in the vicinity of the lower shear layer show the vorticity magnitude of the carrier phase for three different levels.

The initialisation and the evolution of the point droplet mixing is shown in Figure 8 for three stages of the flow evolution. Initially the point droplets are randomly distributed within the core of the planar jet and are characterised by Stokes number $St = 0.1$ which is used in all planar jet simulations. The iteration procedure for individual droplet trajectories was the same as the procedure described for the homogeneous and isotropic simulations. For the cases `J1D4S01` to `J1D16S01` the flow field was averaged using four, eight and sixteen cells along the transverse direction of the flow. An illustration of the positioning of the averaging volumes for this family of simulations is provided in Figure 8, where the borders surrounding two of the eight averaging volumes for the case `J1D8S01` are highlighted. These averaging volumes are adjacent to the lower shear layer of the planar jet at $z_1 = \pi/2$.
In addition, the initial specific values of droplet number densities are assumed at the center of each volume. The normalised number density was taken equal to unity for the centermost droplet elements and zero for the half outermost droplet elements. This setup provides us with an assessment of the turbulent diffusion process, given that the transverse and span-wise averaged velocities are negligible and each averaging volume contains a single Lagrangian droplet element. As a result the resolved droplet dispersion across the shear layer is not evident.
The temporal evolution of the number density for each of the averaging volumes, as calculated from the number of individual droplets within the volume, is shown as dots in Figure 7. As expected, the number density for the averaging volume within the jet core starts from unity and decays due to the mixing induced by the fluctuations of the shear layer. The individual droplets start migrating to the outer layers of the jet. The opposite process can be observed within the averaging volume located at the lean side of the shear layer, where droplets migrating from the jet core increase the concentration of the averaging volume. This is indicated by the lower dotted curve of the same figure. For this specific averaging volume, the initial number density is zero and increases during the mixing process. The concentration of the Lagrangian elements is calculated based on Eq. (17). The outcome of the model described by Eq. (17) is shown as solid and dashed curves in the same figure. In this configuration, the model was used assuming that $\lambda = 1$. The results are shown as dashed curves in Figure 7. Although the trend is predicted correctly, the model over-predicts the intensity of diffusion at the initial stages at which the droplets are expected to adapt to the fluctuations of the carrier phase flow.
The second implementation of the model is also shown in Figure 7, where the ratio λ is introduced to account for the dynamic response of the droplet fluctuations (adaptation behaviour, see solid curves). In this implementation, the predictions of the model agree with the results inferred from the DNS of the individual droplets. The adaptation behaviour is accurately described and droplet number density changes due to turbulent diffusion are predicted. However, for higher resolutions, where the resolved droplet motions are more clearly seen, the one-dimensional averaging used above fails to account for resolved motions. The rightmost part of Figure 4 shows the limits of this one-dimensional implementation of the Lagrangian approach where only four, eight and sixteen Lagrangian droplets were used to model the phenomenon.

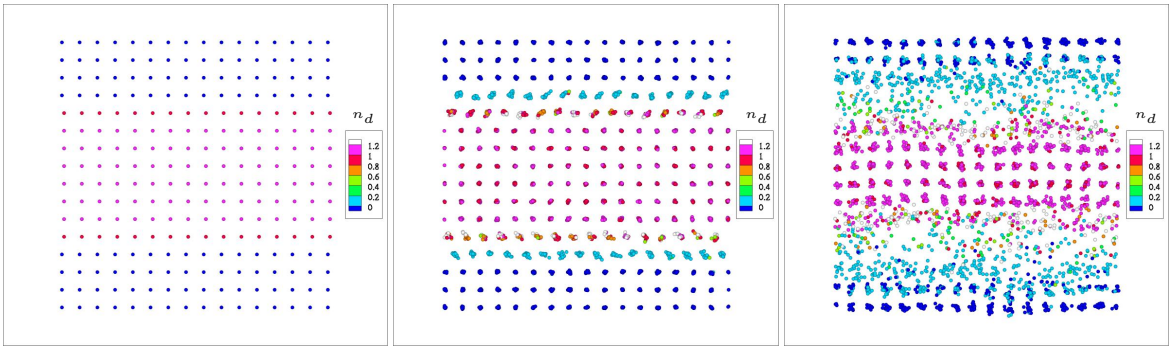

Figure 9. Time evolution of FLA droplets for three time instances at dimensionless times $t^* = 0$, $t^* = 0.270$ and $t^* = 0.575$. Left: The initial distribution of FLA droplets, the number density of which is shown by different colours. Middle: The initial stage of mixing; for the rows of droplets close to the shear layers their number densities start to increase due to unresolved transverse convection, i.e. turbulent diffusion of droplets. Right: The droplets begin to migrate across the shear layer, showing resolved transverse convection.

For the cases `J3D8S01` and `J3D16S01`, the flow field is averaged over $8 \times 8 \times 8$ and $16 \times 16 \times 16$ averaging volumes respectively. This setup involves three-dimensional distribution of FLA droplets which are transported by the average flow field extracted from DNS. The droplet number density is inferred from the integration of Eq. (17) as described earlier. In this setup the full functionality of the model is presented.
The evolution of the lattice-like distribution of the Lagrangian droplet elements is shown in Figure 9. In this figure we show the positions of Lagrangian droplet elements which are transported in the periodic domain of the simulation. These elements start with the same velocities as the carrier phase. They are placed in the centres of the corresponding averaging volume. Their initial normalised number densities n_d are set equal to the normalised number densities of the corresponding averaging volumes. They are set equal to unity close to the core and $n_d = 0$ at the outer layers. As shown in Figure 9, during the initial stages of the flow transition the droplet resolved trajectories are almost uni-directional. However, in the vicinity of the shear layers one can observe an exchange of droplets as described by the second term in Eq. (17). At later stages of jet mixing the droplets change their spatial positions in transverse and span-wise directions following the resolved eddies of the filtered flow field. The results of this combined behaviour of the Lagrangian droplet elements leads to the prediction of the temporal evolution of droplet number density shown in Figure 10 for configurations `J3D8S01` and `J3D16S01`. The evolution of number densities for the averaging volumes adjacent to the shear layer, predicted by averaging the numbers of the individual droplets inferred from the DNS simulation is presented as the dotted curves in Figure 10. The solid curve shows the time evolution of the combined normalised number density for the same averaging volumes as inferred from our model.

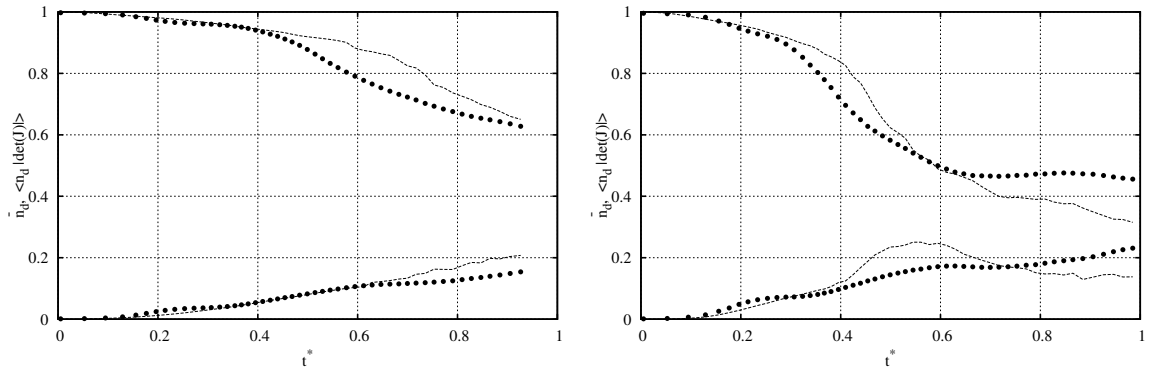

Figure 10. Time evolution of the droplet number density for the cases `J3D8S01` and `J3D16S01` at the two adjacent positions of the planar jet shear layer. Dotted curves: the number density is inferred from the averaging of the number of droplets (over the volume of the averaging cell) predicted by DNS. Dashed curves: Ensemble of the uncompressed FLA droplet number density $< n_d|det(J)| >$ inferred from our model with $\lambda = \mathcal{V}/\mathcal{U}$ Left: 8 averaging volumes in each direction. Right: 16 averaging volumes in each direction.

In contrast to the previous 1D (one-dimensional) analysis we have shown that not only the model successfully predicts the unresolved turbulent diffusion but also captures the changes in the droplet number densities due to

the resolved convection of the dispersed phase. For the comparison of the FLA droplet number densities to the averaged droplet number densities, inferred from the DNS simulations, the normalised spatial average of the number of individual droplets $\overline{n_d}$ was introduced:

$$\overline{n_d} = \frac{4\pi^3}{N} \frac{N_{droplets}}{V_{averaging}} \tag{26}$$

where N is the total number of individual droplets. The DNS results for the individual droplets were compared to the ensemble of the uncompressed droplet number densities $< n_d|det(J)| >$ within an averaging cell. This ensemble number density was introduced in order to obtain a measure of the number of droplets within the averaging volume rather than the local number densities in the vicinity of the FLA droplets [32].

Conclusions

In the work presented in this paper we suggest an extension of the methodology of the Fully Lagrangian Approach that allows us to implement this extended methodology to spatially filtered solutions of turbulent flow fields encountered in the LES analysis of turbulent flows. The original FLA methodology is enhanced by introducing the diffusion term which describes the unresolved dispersion of droplets across the streamlines of the filtered flow field. The introduction of the concept of turbulent diffusion in FLA requires the calculation of the Laplacian of the filtered droplet number density. The calculation of the spatial derivatives for the droplet number densities is performed by projecting the FLA solution on the Eulerian mesh, resulting in a hybrid Lagrangian-Eulerian approach to the problem.
The results of simulations for a statistically significant number of individual droplets described by DNS of droplets in turbulent flow fields were compared with the results retrieved from the implementation of the suggested model using the filtered DNS solution. As follows from our analysis, the hybrid model captures accurately the phenomenon of turbulent mixing in shear flows.

Acknowledgements

The authors are grateful to EPSRC (grants EP/K005758/1 and EP/M002608/1) for the financial support of this project.

Nomenclature

B	empirical constant [-]
c_S	Smagorinsky constant [-]
d_d	droplet diameter [m]
f_i	drag force [kg m s^{-1}]
F_{turb}	number density turbulent flux [m^{-2} s^{-1}]
J	Eulerian to Lagrangian transformation Jacobian [-]
k_v	particle fluctuation energy [m^2 s^{-2}]
k_{sgs}	sub-grid turbulent kinetic energy [m^2 s^{-2}]
L	planar jet width [m]
m_i	droplet mass [kg]
n_d	droplet number density [m^{-3}]
S	rate of strain tensor [s^{-1}]
t	time [s]
t_0	reference time [s]
t^*	dimensionless time [-]
U_i	carrier phase velocity [m s^{-1}]
V_i	droplet velocity [m s^{-1}]
V_e	element volume [m^3]
x_i^d	droplet position [m]
$\mathcal{L}$	characteristic length [m]
$\mathcal{U}$	characteristic velocity [m s^{-1}]
Re_d	droplet Reynolds number [-]
Re_D	jet Reynolds number [-]
Re_T	Taylor Reynolds number [-]
St	droplet Stokes number [-]
δ_m	mixing layer momentum thickness [m]
Δ	element size [m]
ΔU	planar jet velocity difference [m s^{-1}]
ϵ	dissipation rate [m^2 s^{-3}]
λ	ratio of particle to carrier phase fluctuation energy [-]

λ_T	Taylor microscale [m]
μ_c	carrier phase dynamic viscosity [kg m^{-1} s^{-1}]
ν_t	turbulent viscosity [m^2 s^{-1}]
ρ_d	droplet material density [kg m^{-3}]
τ_d	droplet relaxation time [s]
ω	Jacobian time rate [s^{-1}]
$\bar{\cdot}$	spatial filter
$< \cdot >$	ensemble average

References

[1] Sazhin, S.S., 2014 , "Droplets and Sprays.", Springer-Verlag London.
[2] Osiptsov, A. N., 2000, Astrophysics and Space Science, 274, pp. 377–386.
[3] Sazhina, E.M., Sazhin, S.S. and Heikal, M.R., 2000, Combustion Sci. Techolog., 160, pp. 317–344.
[4] Healy, D.P. and Young, J.B., 2005, Proceedings of the Royal Society of London A, 461, pp. 2197–2225.
[5] Meneguz, E. and Reeks, M.W., 2011, J. Fluid Mech., 686, pp. 338–351.
[6] Kaufmann A. et al., 2008, Journal of Computational Physics, 227, pp. 6448–6472.
[7] Danon, H., Wolfshtein, M. and Hetsroni, G., 1977, Int. J. Multiphase Flow, 3, pp. 223–234.
[8] Chan, C.K., Zhang, H.Q. and Lau, K.S., 2000, Comp. Mech., 24, pp. 491–502.
[9] Pakhomov, M.A. and Terekhov, V. I., 2013, Journal of Applied and Technical Physics, 54, pp. 596–607.
[10] Lilly, D.K., 1967, Proc. of IBM Scientific Computing Symp. on Env. Sciences, pp. 195–195.
[11] Clark, R.A., Ferziger, J.H. and Reynolds, W.C., 1979, Journal of Fluid Mechanics, 91, pp.1-16.
[12] Kwak, D.W., Ferziger, J.H. and Reynolds, W. C., 1975, Report TF-5, Thermosci. Div., Dept. Mech. Eng. Stanford Univ.
[13] Deardorff, J.W., 1971, Journal of Comp. Physics, 7, pp. 126–133.
[14] Schumann, U., 1975, Journal of Computational Physics, 18, pp. 376–404.
[15] Bardina, J., Ferzinger, J. and Reynolds, W.C., Jul. 14. -16. 1980, 13th Fluid and Plasma Dynamics Conference, Fluid Dynamics and Co-located Conferences.
[16] Papoutsakis, A., 2008, PhD thesis, Imperial College London.
[17] Kerr, R.M., 1985, Journal of Fluid Mechanics, 153, pp. 31–58.
[18] Givi, P., 1989, Progress in Energy and Combustion Science, 15, pp. 1–107.
[19] Orszag, S.A. and Patterson, G.S., 1972, Physical Review Letters, 28, pp. 76–79.
[20] Mell, W.E., Nilsen, V., Kosaly, G. and Riley, J. J., 1994, Physics of Fluids, 6(3), pp. 1331–1355.
[21] Hussaini, M.Y. and Zang, T.A., 1987, Annual Review of Fluid Mechanics, 19, pp. 339–367.
[22] Wray, A.A., 1986, NASA Ames Research Center, Moffett Field, CA.
[23] Papoutsakis, A., Kronenburg, A. and Jones, W.P., Apr. 2005. 2nd European Combustion Meeting 2005, Louvain-la-Neuve (Belgium).
[24] Stanley, S.A., Sarkar, S. and Mellado, J. P., 1999, Journal of Fluid Mechanics, 450, pp. 0377–0407.
[25] Rogers, M.M., Moser, R.D., 1993, Journal of Fluid Mechanics, 247, pp. 275–320.
[26] Tavoularis, S. and Corrsin, S., 1987, Physics of Fluids, 30(10), pp. 3025–3033.
[27] Wygnanski, I. and Fiedler, H.E., 1970, Journal of Fluid Mechanics, 41, pp. 327.
[28] Pantano, C., 2004, Journal of Fluid Mechanics, 514, pp. 231–270.
[29] Rogers, M.M. and Moser, R.D., 1994, Physics of Fluids, 6(2), pp. 903–922.
[30] Rogers, M.M. and Moser, R.D., 1992, Journal of Fluid Mechanics, 243, pp. 183–226.
[31] Durbin, P.A. and Pettersson, B.A., 2001. "Statistical Theory and Modeling for Turbulent Flows.", John Wiley & Sons.
[32] Reeks, M.W., 2014, Journal of Physics: Conference Series, 530, pp. 1–21.